Conditional Generative Adversarial Network (cGAN) for Synthesis of Digital Histologic Images from Hyperspectral Images

Ling Ma [a,b], Jeremy Sherey [a,b], Doreen Palsgrove [c], Baowei Fei [a,b,d*]

[a] Center for Imaging and Surgical Innovation, University of Texas at Dallas, Richardson, TX;
[b] Department of Bioengineering, University of Texas at Dallas, Richardson, TX;
[c] Department of Pathology, University of Texas Southwestern Medical Center, Dallas, TX
[d] Department of Radiology, University of Texas Southwestern Medical Center, Dallas, TX

*Corresponding author: bfei@utdallas.edu, Website: https://fei-lab.org

ABSTRACT

Hyperspectral imaging (HSI) has been demonstrated in various digital pathology applications. However, the intrinsic high dimensionality of hyperspectral images makes it difficult for pathologists to visualize the information. The aim of this study is to develop a method to transform hyperspectral images of hemoxylin & eosin (H&E)-stained slides to natural-color RGB histologic images for easy visualization. Hyperspectral images were obtained at 40× magnification with an automated microscopic imaging system and downsampled by various factors to generate data equivalent to different magnifications. High-resolution digital histologic RGB images were cropped and registered to the corresponding hyperspectral images as the ground truth. A conditional generative adversarial network (cGAN) was trained to output natural color RGB images of the histological tissue samples. The generated synthetic RGBs have similar color and sharpness to real RGBs. Image classification was implemented using the real and synthetic RGBs, respectively, with a pretrained network. The classification of tumor and normal tissue using the HSI-synthesized RGBs yielded a comparable but slightly higher accuracy and AUC than the real RGBs. The proposed method can reduce the acquisition time of two imaging modalities while giving pathologists access to the high information density of HSI and the quality visualization of RGBs. This study demonstrated that HSI may provide a potentially better alternative to current RGB-based pathologic imaging and thus make HSI a viable tool for histopathological diagnosis.

Keywords: Hyperspectral imaging (HSI), natural-color visualization, conditional generative adversarial network (cGAN), histologic image, computational and digital pathology

1. INTRODUCTION

Hyperspectral imaging (HSI) is a label-free imaging modality that has emerged for medical applications. Several studies have demonstrated that hyperspectral microscopy can improve automated cancer detection in histological slides [1-8]. However, hyperspectral images, in other words hypercubes, have an intrinsic high dimensionality with up to hundreds of bands, thus it is difficult to directly visualize the hypercubes. Digital histologic images acquired with a color camera in an automated whole-slide imaging system has been the routine for pathologists to check the tissue slides and carry out diagnosis. Despite the advantages of using HSI in computational pathology, RGB histologic images are still needed for pathologists to peruse for confirmation. Simple extraction and concatenation of three bands from a hypercube can form a pseudo-RGB image for visualization, but the loss of most spectral information makes it difficult to recover the natural-color appearance of the slide. In our previous works, we developed an HSI-to-RGB transformation method composing of multiple cosine functions, which was based on the spectral response of human eyes [2, 3]. It can generate a pseudo-RGB image from a calibrated hyperspectral image and give an impression of what the tissue slide is like. However, the method does not consider the non-linearity between the transmittance of tissue slide and the values of three channels in the pseudo-RGB image, therefore a certain level of color distortion is inevitable in the pseudo-RGB image. Figure 1 below shows an illustration of a high-dimensional hyperspectral image, its corresponding digital histologic image acquired with a color camera, as well as the generated pseudo-RGB images.

Medical Imaging 2023: Digital and Computational Pathology, edited by John E. Tomaszewski, Aaron D. Ward, Proc. of SPIE Vol. 12471, 124711D · © 2023 SPIE
1605-7422 · doi: 10.1117/12.2653715

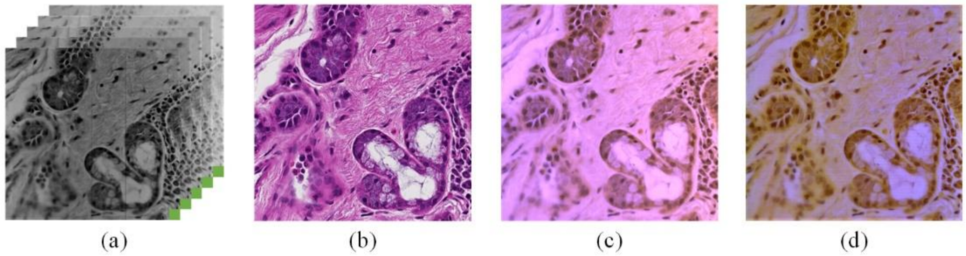

Figure 1. Visualization of histologic images. (a) Hyperspectral histologic image with a high dimensionality, which makes it difficult to directly display the entire image. (b) Digital histologic image acquired with a color camera. (c) A pseudo-RGB image generated from (a) using an HSI-to-RGB transformation function, which was customized according to the spectral response of human eyes. (d) A pseudo-RGB image generated by concatenating 3 bands (525 nm, 582 nm, and 640 nm) from (a).

In the past, several studies tried to synthesize hyperspectral images from RGB images, since RGB images were relatively easier to acquire [9, 10]. However, as the significance of HSI being recognized in recent years, some automated or semi-automated hyperspectral microscopic imaging systems have been developed [6, 11-13], which can implement the acquisition of high-quality digital hyperspectral histologic images for computational pathology purposes. Although two imaging modalities can be integrated into one system, *i.e.*, both the hyperspectral and color cameras can be mounted onto a microscope and acquire both HSI and RGB images simultaneously, it can be more cost effective if only one camera is needed. Since hyperspectral images cover a wide spectrum, where the color information in the RGB images is from, it is feasible to generate natural-color RGB images from hyperspectral images for visualization.

In this study, we propose a natural-color visualization method of hyperspectral histologic images using conditional generative adversarial network (cGAN). The network is able to take a hyperspectral image of any size or objective magnification and generate an RGB image that has a quality very similar to the original digital histologic image taken by a color camera.

2. METHODS

2.1 Histologic slides and hyperspectral dataset

We utilized hematoxylin and eosin (H&E)-stained histological slides as well as their corresponding digital histologic images obtained from four different head and neck squamous cell carcinoma (SCC) patients who underwent routine surgery [14]. Each patient has one slide of normal tissue (N) and one slide of tumor tissue (T), which were imaged using an automated hyperspectral microscopic imaging system [11]. Hyperspectral images were acquired with a 40× objective magnification. The image size was 2,000 pixels × 2,000 pixels × 87 bands, covering the wavelength range of 480-720 nm. In total, 274 hyperspectral images were acquired, where 212 images of 4 slides from two patients were later used in the training data group, 49 images of 2 slide (T and N) from one patient were used in the validation data group, and 13 images of 2 slides (T and N) from one patient were used for testing.

2.2 Data preprocessing

Raw hyperspectral images were firstly calibrated with the white reference images [11]. The real RGB images of the same regions in hyperspectral images were cropped from digital histologic images. To do so we looked at each pseudo-RGB image that was generated from a hyperspectral image using the cosine-based transformation, found the corresponding region in the whole-slide digital histologic image, and cropped an image that had a slightly larger field of view (FOV) than the hyperspectral image. All real RGB images were then registered to their matching hyperspectral images using affine registration with the Oriented FAST and Rotated BRIEF (ORB) feature detector[11, 15]. Then, both hyperspectral and

RGB images were downsampled to generate images with an equivalent objective magnification of 5×, 10×, and 20× and the downsampled images were divided into patches of 100 × 100 pixels × 87 bands. Patches that had more than 50% blank area were excluded from the dataset. In total, we had 60,458 registered patch pairs of 8 slides from 4 patients, and the same patch pair has never been used in the training, validation, and testing at the same time.

2.3 Conditional generative adversarial network (cGAN)

A conditional generative adversarial network was implemented to generate synthetic RGB histologic images from the hyperspectral images of histological slides. Figure 2 shows the diagram of the cGAN we used in this work. It consists of a generator (G) to synthesize RGB images and a discriminator (D) to detect real and synthetic image pairs [9, 16]. Because the input hyperspectral images already contain the spatial information as in the RGB images, the main purpose of the generator is to learn the linear and nonlinear transformation from the spectral dimension to the color channels as well as to correct minor artifacts in some bands. After multiple experiments, we found that using five convolutional layers could yield a reasonable spectrum-to-color conversion, and that using 3×3 kernel in the first convolutional layer with 1×1 kernels in the rest layers could eliminate the artifacts without further blurring the images. Specifically, the 1×1 kernel convolutional layers are used to map the high-dimensional HSI data to the low-dimensional RGB data. A 10% dropout was applied after each convolutional layer. In addition, the fully convolutional architecture can accept any input size, which is beneficial in real application situations. The discriminator consists of several convolutional layers with strides to produce a final feature of size 2×2×2. The details (kernel size, filters, padding) of both the generator and discriminator are given in Figure 2.

The cGAN network was implemented using the Keras API with the TensorFlow backend [17]. During each training iteration, a synthetic RGB image patch was generated from a hyperspectral patch using the generator, and the discriminator was trained on the real and synthetic RGB image patches using the mean absolute error (MAE) loss. Then, the weights of the discriminator were frozen, and the generator was trained using the combined model with the MAE loss and alone with the mean squared error (MSE) loss to the real RGB images. The optimizer was Adam [18] with an initial learning rate of 0.0001. The cGAN was trained for 30 epochs with a batch size of 12.

In this work, we trained the network with the images corresponding to various objective magnifications to increase the robustness of the generator. In our experiments, it was noted that the network trained with the images of one magnification (*e.g.*, 20×) would yield blurred images for the data of other magnifications (*e.g.*, 10× or 40×). Therefore, we trained the cGAN with a mixture of 5×, 10×, and 20× image patches.

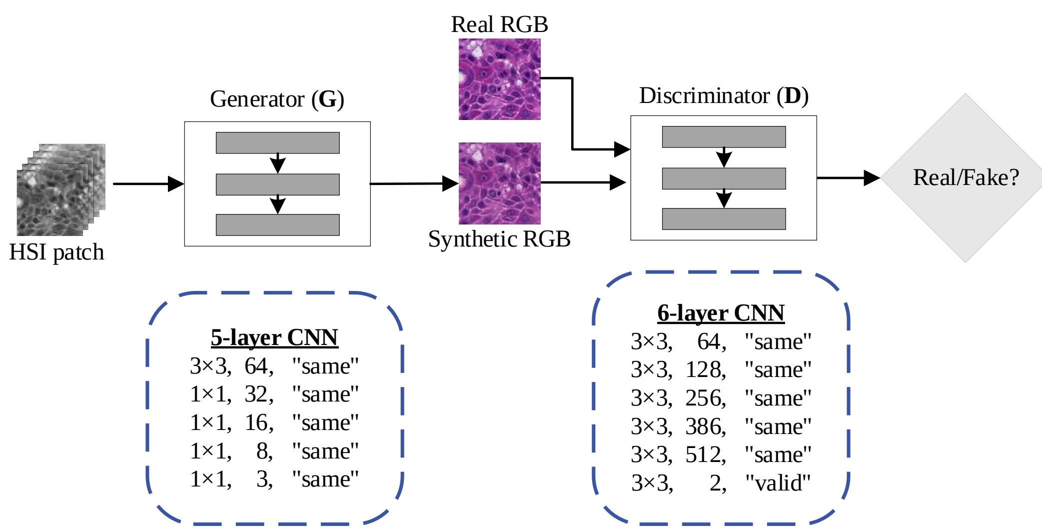

Figure 2. Diagram of HSI-to-RGB transformation using cGAN. The kernel size, number of filters, and padding of the 5-layer generator network architecture as well as the 6-layer discriminator architecture are shown in the dashed blue boxes.

2.4 Evaluation metrics

To quantitatively evaluate the quality of the synthesized RGBs, we firstly use the MATLAB implementations of mean absolute error (MAE), mean squared error (MSE), and peak signal-to-noise-ratio (PSNR) as evaluation metrics. PSNR measures the global intensity difference between the generated RGB and the real RGB histologic images:

$$MAE(\hat{I}, I) = \frac{1}{M \times N \times B} \sum_{k=1}^{B} \sum_{i=1}^{M} \sum_{j=1}^{N} \left| \hat{I}_{ij} - I_{ij} \right| \tag{1}$$

$$MSE(\hat{I}, I) = \frac{1}{M \times N \times B} \sum_{k=1}^{B} \sum_{i=1}^{M} \sum_{j=1}^{N} \left(\hat{I}_{ijk} - I_{ijk} \right)^2 \tag{2}$$

$$PSNR(\hat{I}, I) = 10 \log_{10}(peak\ value^2 / MSE) \tag{3}$$

where $\hat{I}$ is the synthetic RGB image patch and I is the corresponding real RGB image patch, $M = 100$ and $N = 100$ are the spatial dimensions of the RGB image patches, and $B = 3$ is the number of channels.

Then, we used structural similarity index measure (SSIM) [19] and perception-based image quality evaluator (PIQUE) [20] to evaluate the spatial character of the generated RGB histologic images. PIQUE was a method that evaluates the image quality without a reference image; a low score value indicates a high perceptual quality. We calculated PIQUE scores for both the synthetic RGB and real RGB image patches and compared their average image quality. SSIM is calculated between the original and generated images to evaluate how "real" the generated images can be:

$$SSIM(I, \hat{I}) = \frac{(2\mu_I \mu_{\hat{I}} + c_1)(2\sigma_{I\hat{I}} + c_2)}{(\mu_I^2 + \mu_{\hat{I}}^2 + c_1)(\sigma_I^2 + \sigma_{\hat{I}}^2 + c_2)} \tag{4}$$

where μ and σ are the mean and the standard deviation of the RGB histologic images; $c_1 = (0.01 \times L)^2 = 0.0001$ and $c_2 = (0.03 \times L)^2 = 0.0009$ are two constants chosen as the default values dependent on the dynamic range (L) of the image values.

Additionally, in order to evaluate the quality and effectiveness of the synthetic RGB images, we performed image classification using the real and synthetic RGB image patches in the testing data group with a pretrained Inception-based convolutional neural network for cancer detection [11]. Because the network was pretrained on RGB image patches of 10× objective magnification, we only used the 10× patches in the testing group for classification. Each patch was assigned a label of "1" (tumor) or "0" (normal) according to the pathologist's annotations. For the classification of tumor and normal tissue in synthetic and real RGBs, we used the area under the receiver operating characteristic (ROC) curve (AUC), accuracy, sensitivity, and specificity as the evaluation metrics.

$$Accuracy = \frac{TP + TN}{TP + FP + TN + FN} \tag{5}$$

$$Sensitivity = \frac{TP}{TP + FN} \tag{6}$$

$$Specificity = \frac{TN}{TN + FP} \tag{7}$$

where TP, TN, FP, FN are the true positive, true negative, false positive, and false negative.

3. RESULTS

Our proposed cGAN was able to generate natural-color RGB histologic images from hyperspectral images of H&E-stained histological slides, with an 0.6% MSE and 2.1% MAE in the validation data group as well as 0.4% MSE and 1.6% MAE in the testing data group. Table 1 shows the average evaluation results of the validation and testing. Overall, the low error values indicate that our network could synthesize good-quality RGB images from hyperspectral images. The MAE, MSE, and PSNR of 3 objective magnifications did not vary much, which means that our network mostly focused on the spectral mapping and was able to handle images of different magnifications. From the SSIM and PIQUE scores we found that the synthetic RGB images of a higher magnification had a slightly lower similarity to the real RGBs but a higher image quality.

A possible reason is that the depth of field at a higher magnification (*e.g.* 20×) tends to be smaller than that at a lower magnification (e.g. 5×), thus a subtle adjustment of the microscope focus could result in the change of the spatial features in the images. Since the hyperspectral images and RGB histologic images were acquired separately, it was likely that the images acquired at 20× had more disparities than images at 5×. Nevertheless, the larger sensor size of our hyperspectral camera guarantees the overall quality of the synthetic RGB images.

Table 1. Quantitative validation and testing results of the cGAN.

	Magnification	MAE (%)	MSE (%)	PSNR (dB)	SSIM (%)	PIQUE (synthetic)	PIQUE (real)
Validation	5×	2.0 ± 0.6	0.6 ± 0.2	23.1	93.0	42.4	39.3
	10×	2.1 ± 0.6	0.6 ± 0.3	22.8	90.5	41.7	42.0
	20×	2.2 ± 0.7	0.7 ± 0.4	22.6	89.1	34.7	58.0
	Total	2.1 ± 0.6	0.6 ± 0.3	22.8	90.4	38.78	48.4
Testing	5×	1.3 ± 0.3	0.2 ± 0.1	26.1	94.6	39.9	37.7
	10×	1.5 ± 0.4	0.4 ± 0.2	24.7	91.8	40.7	34.3
	20×	1.7 ± 0.4	0.4 ± 0.2	23.9	90.9	35.4	53.3
	Total	1.6 ± 0.4	0.4 ± 0.2	24.7	92.0	38.3	43.1

Figure 3 shows the synthetic and real RGB histologic image patches of a region under different magnifications. The network can handle different magnifications and still guarantee the spatial features. Most fibrous structures and the edge of nuclei were well preserved. Meanwhile, the cellular components stained with hematoxylin and eosin can be clearly differentiated. However, it was noted that the blood (as seen in the 20× and 10× patches in Figure 3) had a darker color in the synthetic images. Nevertheless, most regions showed relatively natural color, which is sufficient to facilitate the visualization of the slide.

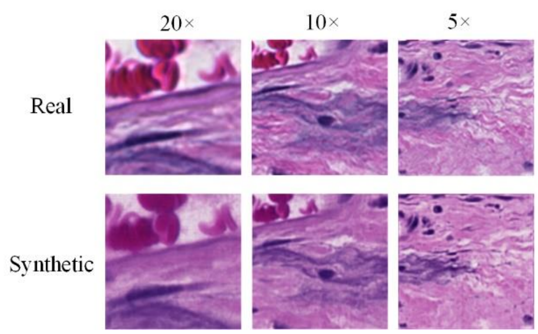

Figure 3. Comparison of real and synthetic RGB histologic images at different objective magnifications.

In Figure 4, we investigate the pathological features of tumor and normal tissues and compare among the real RGB, the synthetic RGB using cGAN, and the synthetic RGB using the cosine-based transformation method. The proposed cGAN worked well for both types of tissues, and critical cancer-related features, such as the atypical mitoses and enlarged nucleoli, are well maintained in the cGAN synthetic images. The major advantage of the cGAN compared to the cosine-based method is the significantly reduced color variation among different slides. In addition, the dark noise and random artifacts in some wavelength bands did not lower the overall quality of the synthetic images.

Finally, the classification of tumor and normal tissue in the testing data group resulted in an 0.94 AUC as well as 0.90 accuracy, 0.92 sensitivity, and 0.88 specificity for the real RGB image patches. Using the synthetic RGB histologic image patches resulted in 0.99 AUC as well as 0.97 accuracy, 0.96 sensitivity, and 0.98 specificity. Because we selected relatively significant tumor and normal regions in the slides to acquire the testing data, using either type of images yielded satisfying results. For the synthetic RGB images, the slight color distortion did not affect the usefulness in a much negative way. In fact, we hypothesize that the cGAN might be able to improve the generalization of the synthetic images, and thus it reduces the overall color variance that is common in real histologic images, which might distract the classifier from distinguishing tumor and normal tissues.

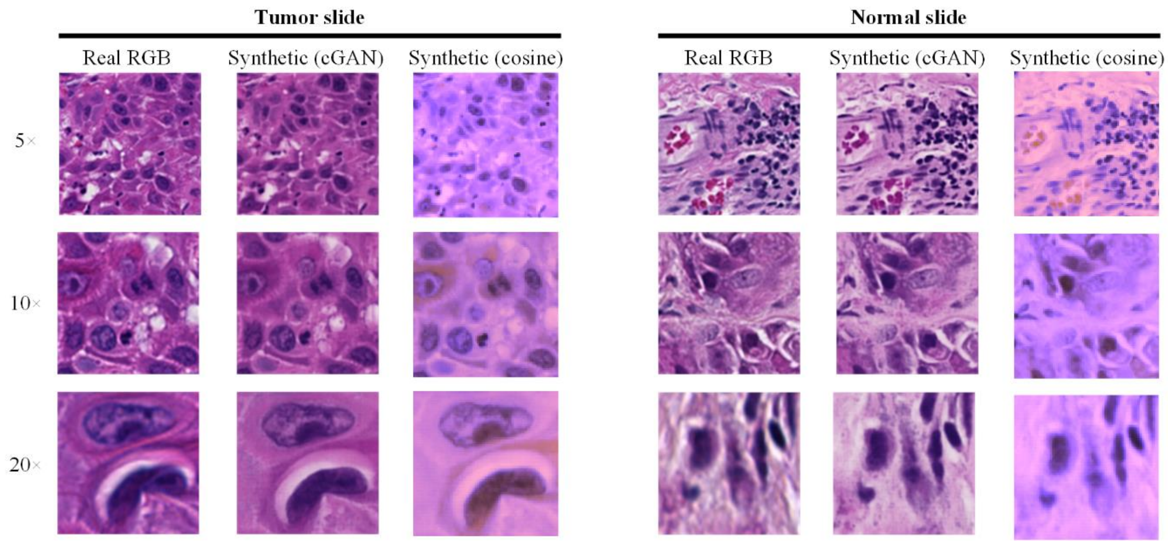

Figure 4. Comparison of real and synthetic RGB image patches of tumor and normal tissues.

4. DISCUSSION AND CONCLUSION

In this work, we developed a conditional generative adversarial network for the purpose of natural-color visualization of hyperspectral images of H&E-stained histological slides. The network can take hyperspectral images as input and generate RGB images with good spatial features and a real color profile. The cGAN was trained using hyperspectral image patches of different magnifications with the corresponding real RGB patches as a condition. Therefore, the proposed method is robust to image size, image noise, and magnifications. In addition, the classification of tumor and normal tissues using the real and synthetic images demonstrated the effectiveness of our synthetic images and the potential improvement of the generalization of image quality.

However, one major limitation of the network is the color distortion of blood in the slides. During the training process, the network tends to generalize the colors in the entire image to reduce the loss. Also, there were very few instances of patches with blood in the training data for the network to learn well. In the future, we will train the network with a larger dataset, including images from more slides and various data augmentations. We also plan to employ the attention mechanism and let the network deal with the different colors of various cellular components. In addition, we will involve some pathologists and get their opinion about the quality of the synthetic images.

In conclusion, our proposed method provides a tool to visualize high-dimensional hyperspectral images. With the value of HSI being more acknowledged in medicine and more automated hyperspectral imaging system being developed, the proposed method can potentially promote the development of fully automated hyperspectral whole-slide scanning systems, allowing HSI for both computational pathology and visualization.

ACKNOWLEDGMENTS

This research was supported in part by the U.S. National Institutes of Health (NIH) grants (R01CA156775, R01CA204254, R01HL140325, and R21CA231911), by the Cancer Prevention and Research Institute of Texas (CPRIT) grant RP190588.

REFERENCES

[1] Ortega, S., Halicek, M., Fabelo, H., Guerra, R., Lopez, C., Lejeune, M., Godtliebsen, F., Callico, G., and Fei, B., "Hyperspectral imaging and deep learning for the detection of breast cancer cells in digitized histological images," Proc. SPIE 11320, 113200V (2020).

[2] Ma, L., Halicek, M., Zhou, X., Dormer, J., and Fei, B., "Hyperspectral microscopic imaging for automatic detection of head and neck squamous cell carcinoma using histologic image and machine learning," Proc. SPIE 11320, 113200W (2020).

[3] Ma, L., Zhou, X., Little, J., Chen, A., Myers, L., Sumer, B., and Fei, B., "Hyperspectral microscopic imaging for the detection of head and neck squamous cell carcinoma on histologic slides," Proc. SPIE 11603, 116030P (2021).

[4] Zhou, X., Ma, L., Brown, W., Little, J., Chen, A., Myers, L., Sumer, B., and Fei, B., "Automatic detection of head and neck squamous cell carcinoma on pathologic slides using polarized hyperspectral imaging and machine learning," Proc. SPIE 11603, 116030Q (2021).

[5] Ortega, S., Fabelo, H., Camacho, R., de la Luz Plaza, M., Callicó, G. M., and Sarmiento, R., "Detecting brain tumor in pathological slides using hyperspectral imaging," Biomed. Opt. Express 9(2), 818-831 (2018).

[6] Ortega, S., Halicek, M., Fabelo, H., Camacho, R., Plaza, M. d. l. L., Godtliebsen, F., M Callicó, G., and Fei, B., "Hyperspectral Imaging for the Detection of Glioblastoma Tumor Cells in H&E Slides Using Convolutional Neural Networks," Sensors 20(7), 1911 (2020).

[7] Ortega, S., Halicek, M., Fabelo, H., Callico, G. M., and Fei, B., "Hyperspectral and multispectral imaging in digital and computational pathology: a systematic review," Biomed. Opt. Express 11(6), 3195-3233 (2020).

[8] Ortega, S., Fabelo, H., Halicek, M., Camacho, R., Plaza, M. d. l. L., Callicó, G. M., and Fei, B., "Hyperspectral superpixel-wise glioblastoma tumor detection in histological samples," Appl. Sci. 10(13), 4448 (2020).

[9] Halicek, M., Ortega, S., Fabelo, H., Lopez, C., Lejeune, M., Callico, G., and Fei, B., "Conditional generative adversarial network for synthesizing hyperspectral images of breast cancer cells from digitized histology," Proc. SPIE 11320, 113200U (2020).

[10] He, Q., and Wang, R., "Hyperspectral imaging enabled by an unmodified smartphone for analyzing skin morphological features and monitoring hemodynamics," Biomed. Opt. Express 11(2), 895-910 (2020).

[11] Ma, L., Rathgeb, A., Mubarak, H., Tran, M., and Fei, B., "Unsupervised super-resolution reconstruction of hyperspectral histology images for whole-slide imaging," J. Biomed. Opt. 27(5), 056502 (2022).

[12] Tran, M., Ma, L., Little, J., Chen, A., and Fei, B., "Thyroid Carcinoma Detection on Whole Histologic Slides Using Hyperspectral Imaging and Deep Learning," Proc. SPIE 12039, 120390H (2022).

[13] Ortega, S., Guerra, R., Díaz, M., Fabelo, H., López, S., Callicó, G. M., and Sarmiento, R., "Hyperspectral Push-Broom Microscope Development and Characterization," IEEE Access 7, 122473-122491 (2019).

[14] Halicek, M., Dormer, J. D., Little, J. V., Chen, A. Y., and Fei, B., "Tumor detection of the thyroid and salivary glands using hyperspectral imaging and deep learning," Biomed. Opt. Express 11(3), 1383-1400 (2020).

[15] Rublee, E., Rabaud, V., Konolige, K., and Bradski, G., "ORB: An efficient alternative to SIFT or SURF," 2011 International Conference on Computer Vision, 2564-2571 (2011).

[16] Mirza, M., and Osindero, S., "Conditional generative adversarial nets," arXiv:1411.1784v1 (2014).

[17] Ketkar, N., [Deep Learning with Python: A Hands-on Introduction] Apress, Berkeley, CA(2017).

[18] Kingma, D. P., and Ba, J., "Adam: A method for stochastic optimization," arXiv:1412.6980 (2014).

[19] Wang, Z., Bovik, A. C., Sheikh, H. R., and Simoncelli, E. P., "Image quality assessment: from error visibility to structural similarity," IEEE Trans. Image Process. 13(4), 600-612 (2004).

[20] Venkatanath, N., Praneeth, D., Bh, M. C., Channappayya, S. S., and Medasani, S. S., "Blind image quality evaluation using perception based features," 2015 Twenty First National Conference on Communications (NCC), 1-6 (2015).